ARTICLE

Check for updates

Segregation-induced strength anomalies in complex single-crystalline superalloys

Andreas Bezold [1✉], Jan Vollhüter[1], Nicolas Karpstein [2], Malte Lenz[2], Aparna P. A. Subramanyam[3,5], Christopher H. Zenk[4], Thomas Hammerschmidt [3], Erdmann Spiecker [2], Mathias Göken[1] & Steffen Neumeier[1]

Pushing the maximum service temperature of aircraft engines and industrial gas turbines is the major pathway to improve their energy efficiency and reduce CO_2 emissions. This maximum is mostly limited by the temperature capability of key-component materials, including superalloys. In this alloy class, segregation of elements facilitates plastic deformation and is generally considered to cause softening during high-temperature deformation. Here, we show that segregation-assisted processes can also lead to strengthening and induce an anomalous increase of the yield strength. Atomic-resolution transmission electron microscopy and density functional theory calculations reveal a segregation-assisted dissociation process of dislocations at precipitate-matrix interfaces in combination with atomic-scale reordering processes. These processes lead to an inhibition of athermal deformation mechanisms and a transition to stacking fault shearing, which causes the strengthening effect. Unraveling these elementary mechanisms might guide a mechanism-based alloy design of future superalloys with enhanced high-temperature capabilities.

[1] Department of Materials Science & Engineering, Institute I: General Materials Properties, Friedrich-Alexander-Universität Erlangen-Nürnberg, Martensstr. 5, Erlangen 91058, Germany. [2] Department of Materials Science & Engineering, Institute of Micro- and Nanostructure Research, and Center for Nanoanalysis and Electron Microscopy (CENEM), Friedrich-Alexander-Universität Erlangen-Nürnberg, IZNF, Cauerstr. 3, Erlangen 91058, Germany. [3] Interdisciplinary Centre for Advanced Materials Simulation (ICAMS), Ruhr-Universität Bochum (RUB), Universitätsstr. 150, 44780 Bochum, Germany. [4] Department of Materials Science & Engineering, Institute II: Materials Science and Metals Engineering (WTM), Friedrich-Alexander-Universität Erlangen-Nürnberg, Martensstr. 5, Erlangen 91058, Germany. [5]Present address: Theoretical Division, Los Alamos National Laboratory, Los Alamos, NM 87545, USA. ✉email: andreas.bezold@fau.de

Despite all measures to reduce greenhouse gas emissions, they keep increasing due in part to the ever-growing air traffic and the increasing demand for energy. Because of the necessity to reduce the environmental impact, there is an urgent need to improve the energy efficiency of gas turbines by increasing their operating temperature. From a materials science point of view, high-performance structural alloys with improved temperature capabilities are needed. As of now, Ni-base super-alloys are the only materials with a property profile which simultaneously meets the challenging requirements for components in the hottest and mechanically most stressed sections of gas turbines: a high elevated-temperature strength and ductility as well as an excellent oxidation and corrosion resistance. Super-alloys derive their excellent high-temperature mechanical properties from their characteristic two-phase microstructure: a high volume fraction of γ' precipitates with the ordered L1$_2$ crystal structure is coherently embedded in a face-centered cubic (fcc) γ matrix phase, which allows operating temperatures of up to 85% of the alloys' melting temperature. Originating from Ni-Al-Cr alloys, advanced superalloys possess more than ten different alloying elements to improve specific strengthening mechanisms such as precipitation (e.g. Al, Ti, Ta, Nb), solid-solution (e.g. Mo, W, Ru, Re) or grain-boundary strengthening (e.g. C, B, Zr). Furthermore, Cr and Si are added for oxidation and corrosion resistance. In addition to Ni-base superalloys, the recent rediscovery[1] of a metastable γ' phase in the ternary Co-Al-W system enabled the development of similarly complex superalloys based on Co or intermediate CoNi-base alloys as potential high-temperature structural alloys[2–5].

While the yield strength of most metallic elements and alloys decrease with increasing temperature, an anomalous increase of the yield strength is observed in some pure elements (e.g. Be[6]), some disordered phases (e.g. Cu-10Al[7]) and multiple inter-metallic compounds[8–12] (e.g. TiAl, Ni$_3$Al). Especially the yield strength anomaly (YSA) of the L1$_2$-ordered γ' phase has received widespread attention since the 1960s as the yield strength peak can reach temperatures of over 800 °C and is also observed in more complex two-phase γ/γ' superalloys. In both single- and two-phase alloys, the YSA is attributed to the thermally activated locking of linear defects[13–15], which are called dislocations and are the carrier of plastic deformation. Due to the ordered nature of the L1$_2$ crystal structure, typical dislocations in the fcc-γ matrix phase of the type a/2[110]{111} destroy the local order of the L1$_2$ structure and cause energetically unfavorable nearest-neighbors. Therefore, these dislocations typically have to shear pairwise through the γ' phase so that the trailing dislocation of the two restores the ordered phase to its original configuration. The high-energy fault between these dislocation pairs is called anti-phase boundary (APB). With increasing temperature, the cross-slip probability of the leading dislocations from an {111} to an energetically more favorable {100} plane increases, which locks the dislocation configuration and induces the YSA[13–15]. Besides the activation of the {100} glide plane[16], dislocation bypassing mechanisms[17,18] or the transition to shearing under the formation of stacking faults and subsequent microtwinning[19] cause a drop of the yield strength in Ni-base superalloys at even higher temperatures. Interestingly, the transition from shearing by APB-coupled dislocations to stacking-fault shearing does not lead to a significant decrease of the yield strength in Co-base and CoNi-base superalloys[17,20–22] and might even be associated with an anomalous increase[23]. As reported recently[22,24], this transition depends not only on the temperature but also on the test duration (or strain rate), suggesting that diffusive processes play an important role.

In recent years, state-of-the-art atomic-scale characterization techniques such as high-resolution scanning transmission electron microscopy (HRSTEM) and atom probe tomography revealed the significance of segregation of solute atoms to linear and planar defects in the γ' precipitates[25–32]. By lowering their defect energies, these segregation processes facilitate the propagation of dislocations[33,34]. However, the role of such diffusive processes in the nucleation of planar defects is unclear.

Herein, we reveal a segregation-assisted transition of the dominant deformation mechanism as a function of temperature and strain rate using advanced atomic-scale structural and chemical investigations by HRSTEM in combination with density functional theory (DFT) calculations. The change of the acting mechanism is found to be associated with a strengthening effect and leads to a yield strength anomaly in superalloys. The unveiling of this mechanism and the beneficial strengthening effect could guide alloy design to develop superalloys with specific advantageous deformation mechanisms at the target application temperature.

Results

Compression experiments and defect structures. The high-temperature strength of a single-crystalline CoNi-base superalloy called ERBOCo-4 (Co-32Ni-8Al-5.7W-6Cr-2.8Ti-1.8Ta-0.4Si-0.1Hf (at.%)) was assessed using constant strain rate compression tests. Figure 1 reveals the anomalous yielding behavior of ERBOCo-4 and the corresponding defect structures of compression deformed specimens, which were interrupted at the yielding point, which is in general defined to be at a plastic strain of 0.2%. An overview of representative defect structures at all investigated conditions is shown in the Supplementary Fig. 1. At either low temperatures or high strain rates (Fig. 1a or Fig. 1b, c, respectively), shearing by APB-coupled dislocation pairs is observed as indicated by the red background in Fig. 1a–c and exemplarily shown in Fig. 1d after an interrupted compression test at 800 °C and a strain rate of $10^{-5}\,s^{-1}$. The leading dislocations of most of these dislocation pairs cross-slip on a {001} plane and form immobile locks. Additionally, dislocations are also active in the matrix channels and are able to bypass the γ' precipitates via the Orowan mechanism as analyzed previously[22]. With increasing temperature or decreasing strain rate, the yield strength increases anomalously (Fig. 1a–c). Simultaneously, the dominant shearing mechanism transitions to shearing under the formation of stacking faults, predominantly identified as superlattice extrinsic stacking faults (SESFs), as exemplarily shown in Fig. 1e (blue background in Fig. 1a–c). If the temperature increases or the strain rate decreases even further, stacking faults evolve into microtwins as confirmed by the additional diffraction spot in the inset of Fig. 1f. Furthermore, individual uncoupled matrix dislocations shear into the γ' precipitates, leaving extended APBs in their wake (see Supplementary Fig. 1i). This transition is accompanied by a strong decrease of the yield strength (Fig. 1a, c).

Atomic-scale structural and chemical investigations. As proposed recently[22], the dissociation of a dislocation at a γ/γ' interface might temporarily prevent its further progression. The effectiveness of this inhibition was suggested to depend on the time available for segregation of alloying elements, which enables the leading Shockley partial to shear further into the γ' precipitate until it reaches an equilibrium dissociation distance. Thus, the atomic-scale structure and chemical segregation profile of such a dissociated interfacial dislocation was characterized through HRSTEM and energy-dispersive X-ray spectroscopy (EDS) (Fig. 2). Due to the dissociation of an fcc matrix dislocation of the type $a/2\langle01\bar{1}\rangle$, a stacking fault arises between the two partial dislocations. As indicated in the inset of Fig. 2a, the nature of the stacking fault is intrinsic as the stacking sequence changes from
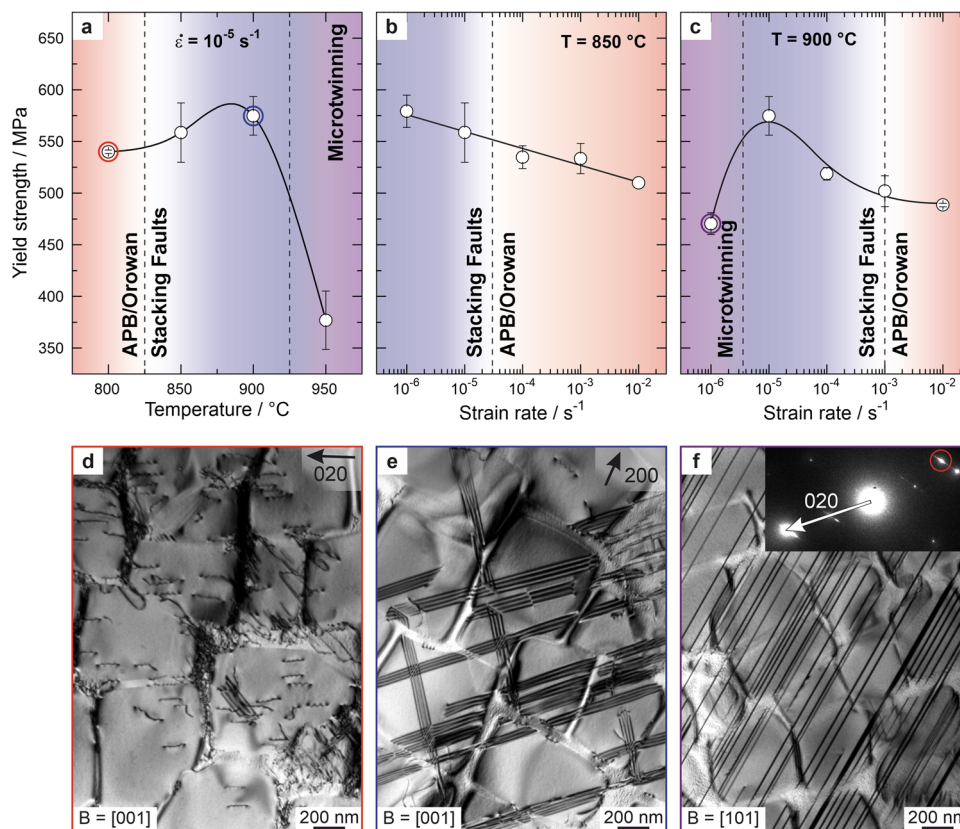
Fig. 1 Anomalous yielding behavior and defect structures. a Yield strength of single-crystalline ERBOCo-4 as a function of temperature at a strain rate of 10^{-5} s^{-1}. **b**, **c** Yield strength as a function of strain rate at a temperature of 850 °C and 900 °C, respectively. The transition from shearing by APB-coupled dislocation pairs/Orowan looping (red) to stacking fault shearing (blue) and microtwinning (purple) is indicated. Error bars represent the standard deviation. Exemplary transmission electron microscopy (TEM) bright-field images of the main deformation mechanisms are shown in (**d-f**): **d** shearing by APB-coupled dislocation pairs, **e** shearing under the formation of stacking faults and **f** microtwinning. Images were taken in two-beam conditions close to the (**d**, **e**) [001] and (**f**) [101] zone axis.

ABCABCA to ABC||BCAB. The trailing (orange) and leading (blue) dislocations are separated by a distance of about 8 nm. Burgers circuits around these partial dislocations reveal a projected displacement of $a/12[\bar{1}1\bar{2}]$ and $a/6[\bar{1}1\bar{2}]$ for the trailing and leading dislocations, respectively. As shown in the Supplementary Note 1, these projected displacements in combination with the shear stress direction resulting from compressive loading along the [001] direction lead to a Burgers vector of either $a/6[2\bar{1}1]$ or $a/6[12\bar{1}]$ for the trailing partial dislocation and $a/6[\bar{1}1\bar{2}]$, $a/3[2\bar{1}1]$ or $a/3[12\bar{1}]$ for the leading partial dislocation. Since compact dislocations with a Burgers vector of $a/3[2\bar{1}1]$ or $a/3[12\bar{1}]$ would not be favored during compressive deformation in [001] direction and the leading dislocation is not dissociated into a complex dislocation arrangement (similar to what is observed during tensile deformation[35]) (see Fig. 2a), its Burgers vector has to be $a/6[\bar{1}1\bar{2}]$. In order to determine whether the intrinsic stacking fault has a complex or superlattice structure, the TEM foil was tilted to the $[\bar{1}2\bar{1}]$ zone axis (Fig. 2d). As shown in the Bragg-filtered inset, no distinctive shift is observed in the superlattice contrast, which reveals that the fault is not a complex intrinsic stacking fault (CISF) but a superlattice intrinsic stacking fault (SISF)[36]. However, the experimentally identified Shockley partial dislocation of the type $a/6[\bar{1}1\bar{2}]$ would introduce a CISF and not the observed SISF. This apparent discrepancy and the underlying formation mechanism of the SISF will be rationalized in the discussion section. Another example of one of these dissociated dislocations and lower magnification images are presented in Supplementary Note 2.

HRSTEM-EDS mappings of the dissociated dislocation reveal the enrichment of Co and Cr and the depletion of all other alloying elements along the planar fault (Fig. 2e, f). This segregation behavior is also observed on one side next to it (left of the fault in Fig. 2e), which leads to a loss of the superlattice structure in this region as indicated in Fig. 2a. Interestingly, as indicated in the Cr mapping in Fig. 2e, the segregated region has an angle of about 35° between the stacking fault and the other boundary of this area, which is perpendicular to the original edge of the γ′ precipitate. The line scan across the stacking fault (indicated in the Co mapping in Fig. 2e) quantifies the degree of segregation (Fig. 2f). The enrichment of Co of about 10 at.% is compensated by a similar depletion of Ni. The strong segregation of Cr, from 4 at.% to 10 at.%, is balanced by a depletion of W, Al, Ti and Ta. Due to the segregation of Co and Cr to the region on the left of the stacking fault, the segregation profiles of all alloying elements are asymmetrical.

Since shearing under SESF formation is the dominant shearing mechanism at the peak temperature of the yield strength anomaly, an SESF was also investigated to unravel its complete nucleation sequence after the leading Shockley partial of the dissociated matrix dislocation shears into the γ′ precipitate. As shown in the overview image and the inset in Fig. 3a, the SESF is still comparatively short (< 20 nm) and its extrinsic nature is confirmed by the change of its stacking sequence from ABCABCA to ABC|B|ABC. Similar to the observation of the dissociated dislocation in Fig. 2, the superlattice structure is lost on one side of the fault as indicated in Fig. 3a. The two trailing
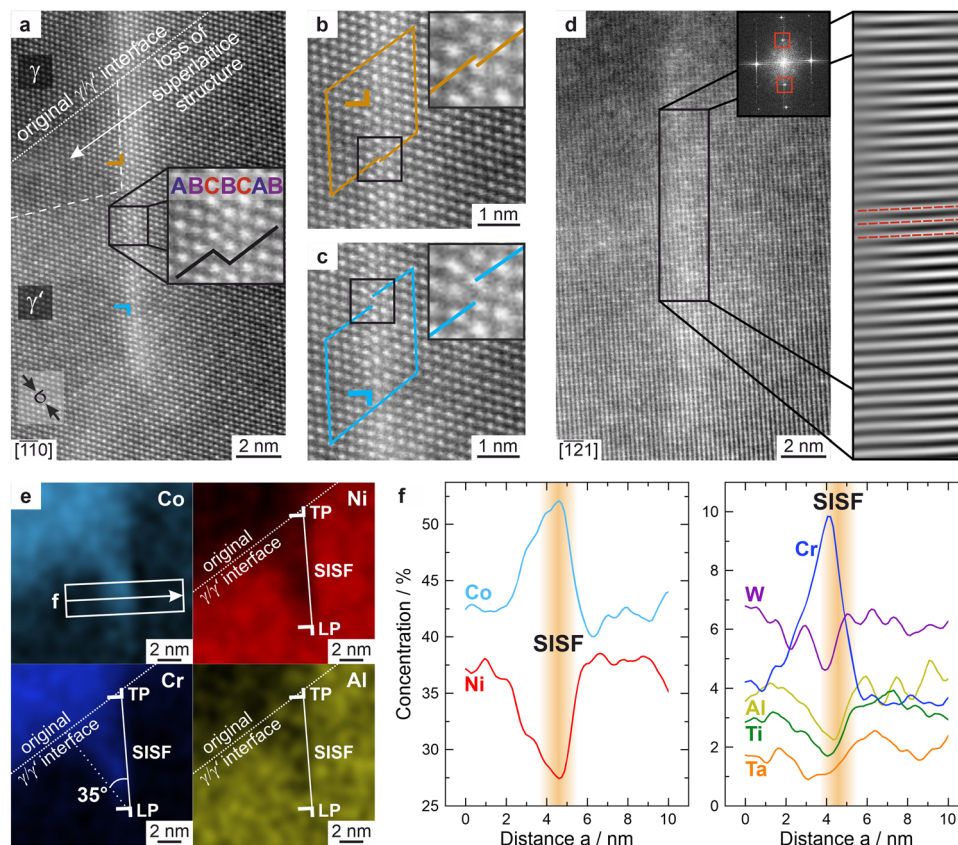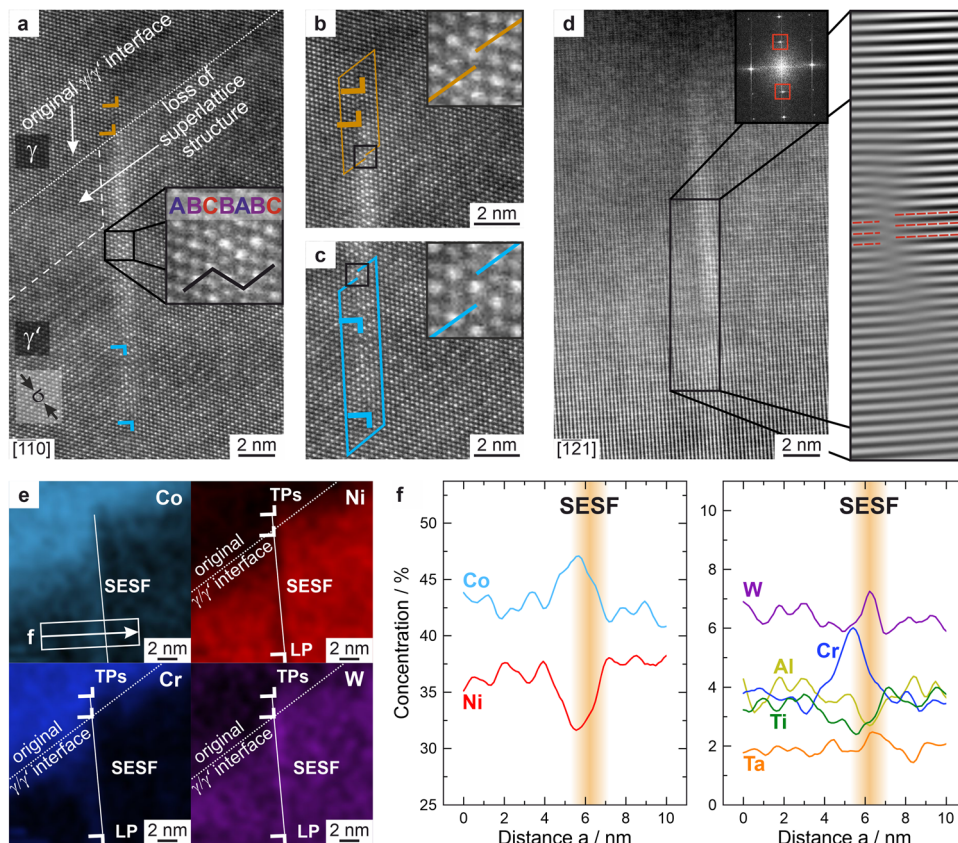
Fig. 2 Atomic-scale structural and chemical characterization of a dissociated interfacial dislocation. a Overview HRSTEM image of the dissociated interfacial dislocation. The regions of the γ and γ′ phases are indicated by the white dotted line. The intrinsic nature of the fault is shown in the inset. **b** Burgers vector circuit around the trailing dislocation at the γ/γ′ interface. The inset reveals the projected displacement of $a/12[\bar{1}1\bar{2}]$. **c** Burgers vector circuit around the leading dislocation. The inset reveals the projected displacement of $a/6[\bar{1}1\bar{2}]$. **d** HRSTEM image of the dissociated dislocation in the $[\bar{1}21]$ zone axis. The Bragg-filtered inset using the $\pm(101)$ superlattice reflection (red squares) reveals the superlattice nature of the stacking fault. **e** Lower magnification HRSTEM-EDS mapping of Co, Ni, Cr and Al. The position of the leading partial (LP), trailing partial (TP), fault (SISF) and the original γ/γ′ interface are indicated in the Ni, Cr and Al mappings. **f** EDS Linescan across the intrinsic stacking fault as indicated in the Co mapping in (**e**).

dislocations (orange) are still located at the γ/γ′ interface, while both leading partial dislocations sheared into the γ′ precipitate. As shown in the insets of Fig. 3b, c, the analysis of the Burgers vector circuit around the trailing and leading partial dislocations yields projected displacements of $a/6[\bar{1}1\bar{2}]$ and $a/3[\bar{1}1\bar{2}]$ - so exactly twice as much compared to the trailing and leading partial dislocations in Fig. 2. Hence, both trailing dislocations are Shockley partial dislocations of the type $a/6[2\bar{1}1]$ or $a/6[12\bar{1}]$, while the leading dislocations are both Shockley partial dislocations of the type $a/6[\bar{1}1\bar{2}]$. The Bragg-filtered image of this SESF in the $[\bar{1}21]$ zone axis reveals a displacement between both leading Shockley partial dislocations confirming the complex intrinsic nature of the stacking fault between both leading Shockley partial dislocations. Additionally, no displacement of the central atomic columns is observed along the remaining stacking fault confirming that the extrinsic stacking fault is indeed an SESF and not two CISFs stacked above each other[36].

Similar to the dissociated dislocation, HRSTEM-EDS mappings of the SESF reveal that not only the planar fault itself but also an area on one side of it close to the γ/γ′ interface is enriched in Co and Cr as shown in Fig. 3e. In contrast, W enrichment is only observed along the SESF (white line). These local differences are quantified in Fig. 3f by a line scan across the SESF as indicated in the Co mapping in Fig. 3e. Compared to the dissociated interfacial dislocation in Fig. 2, the magnitude of enrichment/ depletion is lower by a factor of approximately 2. While the area next to the SESF is enriched in Co and Cr, it is depleted in Ni and

Ti. The peak of the elemental segregation is about 0.6 nm on the left of the SESF. Furthermore, the elements W and Ta segregate only to the SESF and their enrichment is compensated by a depletion in Al.

Density functional theory calculations. Theoretically, shearing by single Shockley partial dislocations of the type $a/6[\bar{1}1\bar{2}]$ leads to the formation of a high-energy CISF in the L1$_2$-ordered γ′ precipitates. Nevertheless, the SF between the Shockley partial dislocations of the dissociated interfacial dislocation was determined to possess a non-complex structure (Fig. 2d). In the literature, it has been hypothesized that the high-energy CISF should be able to reduce its energy by reordering to an SISF[37]. However, such a direct reordering is not possible as the unfavorable nearest-neighbor violations cannot be erased without an additional shear displacement. Thus, a CISF reordering into an SISF configuration will inherently create an APB on an adjacent plane as shown in Supplementary Note 3. To clarify the likelihood of such a planar fault transformation, DFT calculations were conducted on simulation cells with corresponding planar fault configurations as shown in Fig. 4a, b. The chemical composition in the simulation cells is based on Ni, Co, and Al as these are the dominant species in the experimental sample. The difference in the DFT total energies of the two configurations (with the same number of atoms and the same stoichiometry) corresponds directly to the difference in the formation energies of the CISF and the SISF + APB configuration. The computed DFT

Fig. 3 Atomic-scale structural and chemical characterization of an SESF. a Overview HRSTEM image of the SESF. The regions of the γ and γ′ phases are indicated by the white dotted line. The extrinsic nature of the fault is shown in the inset. **b** Burgers vector circuit around the trailing dislocations. The inset reveals the projected displacement of $a/6[\bar{1}1\bar{2}]$. **c** Burgers vector circuit around the leading dislocations. The inset reveals the projected displacement of $a/3[\bar{1}2\bar{1}]$. **d** HRSTEM image of the SESF in the $[\bar{1}2\bar{1}]$ zone axis. The Bragg-filtered inset using the ±(101) superlattice reflection (red squares) reveals the complex nature of the leading segment. **e** Lower magnification HRSTEM-EDS mapping of Co, Ni, Cr and W. The position of the leading partials (LP), trailing partials (TP), fault (SESF) and the original γ/γ′ interface are indicated in the Ni, Cr and W mappings. **f** EDS Linescan across the extrinsic stacking fault as indicated in the Co mapping in (**e**).
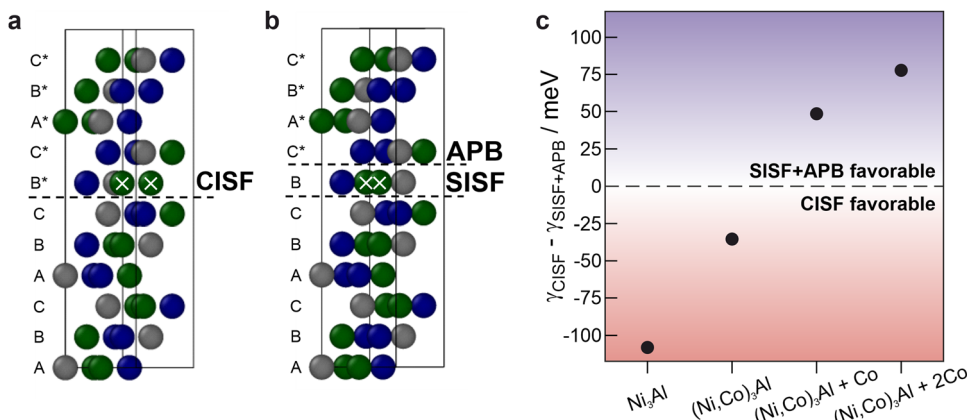
Fig. 4 Density functional theory calculations. The ordered $(Ni,Co)_3Al$ supercell with the introduced (**a**) CISF and (**b**) APB + SISF structures. The blue, green, and gray atoms correspond to Co, Ni, and Al atoms respectively. **c** The energy differences between the defect supercells reveal the relative stability of the CISF and the SISF + APB configurations. To simulate segregation, the Ni atoms marked with white crosses in (**a**, **b**) are replaced by Co atoms.

energies in Fig. 4c show that the CISF configuration is energetically favorable in Ni_3Al and $(Ni,Co)_3Al$. Segregation of Co, which is simulated by increasing the Co concentration at the fault plane (marked with white crosses in Fig. 4a, b), destabilizes the CISF and stabilizes the SISF + APB configuration. As the energy differences between the segregated SISF + APB and CISF configurations are sizeable, a clear picture emerges at 0 K. However,

investigating how these energy differences might be influenced by finite temperature conditions is a subject for future research.

Discussion

During high temperature deformation of γ′ strengthened superalloys, various deformation mechanisms can occur depending on

numerous factors such as alloy composition, grain orientation, applied stress, temperature and deformation rate[24,27,32,38–42]. Recently, elemental segregation to dislocations at the γ/γ′ interfaces was also proposed to influence the type of the occurring shearing mechanism[22,34]. Based on the results in the present and a previous study[22,24], the acting shearing mechanism transitions from athermal shearing by APB-coupled dislocation pairs to shearing under stacking fault formation with increasing temperature, increasing plastic strain and/or decreasing strain rate, i.e. conditions with increasing effective diffusion length. Hence, these systematic investigations confirm the general significance of segregation processes on the acting deformation mechanisms. Based on the experimental HRSTEM(-EDS) investigations and the DFT calculations, the reason for this behavior, i.e., a segregation-assisted nucleation theory for superlattice extrinsic stacking fault shearing, which causes the transition in the deformation mechanism, is proposed in the following. The underlying nano- and atomic-scale segregation, shearing and reordering processes of this proposed mechanism is shown in Fig. 5.

A dissociated matrix dislocation with a combined Burgers vector of a/2[01$\bar{1}$] approaches the γ/γ′ interface (Fig. 5a–c). The leading Shockley partial dislocation of the type a/6[$\bar{1}$1$\bar{2}$] shears into the γ′ precipitate and creates a high-energy CISF, while the trailing Shockley partial dislocation of the type a/6[12$\bar{1}$] remains trapped at the γ/γ′ interface (Fig. 5d–f). Subsequently, Co and Cr segregate to the CISF, which decreases its energy and facilitates the propagation of the leading Shockley partial dislocation (Fig. 5e). If the CISF is sufficiently enriched by Co and Cr, the planar fault energy can be further reduced by atomic reordering processes along the [$\bar{1}$10] direction as revealed by the DFT calculations in Fig. 4 and indicated by the red arrows in Fig. 5e, f (see Supplementary Note 3 for more details), which shift the unfavorable nearest-neighbor relationships to the adjacent (11$\bar{1}$) plane and transform the CISF to an SISF + APB configuration (Fig. 5g–i). As known from the literature[28,37,43], Co and Cr segregate even more strongly to the APB than to the SISF leading to an asymmetrical segregation profile (Fig. 5h). Subsequently, the APB migrates to the (1$\bar{1}$0) plane by additional atomic reordering processes along the [$\bar{1}$10] direction to reduce its total area and thus its overall energy as indicated in Fig. 5h–j. Due to this migration, the resulting configuration does not lead to a shift in the superlattice contrast, when it is observed from the [$\bar{1}$21] zone axis, which is consistent with the experimental observations in Fig. 2d. During the migration process to the (1$\bar{1}$0) plane, the APB attracts more Co and Cr atoms leading to a γ-like environment next to the stacking fault. Due to the proximity to the γ matrix channel and the absence of any local composition variations next to the γ-like environment, the enrichment of Co and Cr in this γ-like environment is facilitated by diffusion from the γ matrix channel. The boundary of this region on the (1$\bar{1}$0) plane has a 35.26 ° angle to the (11$\bar{1}$) habit plane of the SISF, which is in very good agreement with the experimentally determined angle of 35 ° in Fig. 2e. At this point, the dislocation and fault configuration is immobile and effectively pinned as shown below until a second Shockley partial dislocation approaches it as indicated in Fig. 5k. As one side of the stacking fault (the area to the left of the SISF in Fig. 2a) is strongly enriched in Co and Cr forming a more γ-like region, the Shockley partial dislocation shears into the γ′ precipitate preferentially on this side and creates a CISF in its wake, which again reorders into an SISF + APB configuration (Fig. 5l). By migrating to an (1$\bar{1}$0) plane to again reduce the overall fault area and defect energy, both APBs are annihilated due to their same translation vector and a perfect SESF remains (Fig. 5m–o). Subsequently, the leading Shockley partial dislocations continue to shear through the γ′ precipitates via the so-called *Kolbe*

mechanism[44,45] (Fig. 5n): the CESF created by the Shockley partial dislocations reorders to an energetically more favorable SESF, whose energy is further reduced through segregation of Co and Cr, which facilitates the propagation of the Shockley partial dislocations and the SESF. As confirmed recently[36] and verified in this work, one of the Shockley partial dislocations is slightly ahead of the other one leading to a complex intrinsic leading segment as shown in Fig. 5n.

While this proposed mechanism can explain the atomic-scale structural and chemical observations, the question remains whether the configuration observed in Fig. 2 and illustrated in Fig. 5k is indeed locked until a second Shockley partial dislocation approaches it. For these considerations, it has to be noted that plastic deformation in two-phase γ/γ′ superalloys with a positive lattice misfit, i.e., a larger lattice parameter of the γ′ precipitate phase compared to the one of the γ matrix phase, is initiated in the horizontal γ′ matrix channels under compressive deformation in the [001] direction. Indeed, all the investigated dissociated dislocations were also found at the horizontal γ/γ′ interfaces. Here, the horizontal γ matrix channels and γ/γ′ interfaces refer to the matrix channels and interfaces perpendicular to the loading direction. Hence, the force balance for the dislocation configuration is set up for a dissociated dislocation at the horizontal γ/γ′ interfaces, with the leading Shockley partial dislocation already sheared into the γ′ precipitate to match the configuration observed in Fig. 2 and proposed in Fig. 5k. As shown in detail in Supplementary Note 4, the leading Shockley partial dislocation can then only break away from the trailing one, when the following condition is fulfilled:

$$\tau b > \gamma_{\text{SISF}} + \gamma_{\text{APB}} + F_{\text{f}} + F_{\text{misfit}}, \tag{1}$$

where τ is the resolved shear stress, b is the magnitude of the Burgers vector of the Shockley partial dislocation, γ_{SISF} is the SISF energy, γ_{APB} is the APB energy and F_{f} is the friction force on the Shockley partial dislocation per unit length. Additionally, the edge component of the leading (and also the trailing) Shockley partial can compensate the acting coherency stresses, which requires overcoming an additional force per unit length F_{misfit}. Given that the distance of the leading Shockley partial and the original γ/γ′ interface is about 8 nm, this additional force is considered to be negligible for the leading Shockley partial dislocation.

A similar force balance was derived previously by Titus et al.[33] for SISF-based shearing. In the present study, the highest measured yield strength $R_{\text{p},0.2}$ is 579 MPa (for $T = 850$ °C and $\dot{\varepsilon} = 10^{-6}$ s^{-1}). Thus, the leading Shockley partial dislocation can only break away if the sum of the planar fault energies and the friction force is smaller than $\tau b = R_{\text{p},0.2}m_{\text{l}}b = 579\,MPa \cdot 0.471 \cdot 1.46 \cdot 10^{-10}m = 40\,mJ\,m^{-2}$, where m is the Schmid factor (with $m_{\text{l}} = 0.471$ for the leading and $m_{\text{t}} = 0.236$ for the trailing Shockley partial dislocation). For CoNi-base superalloys, the energy of APBs is assumed to be larger than the energy of SISFs, whereby the ratio between these energies is further increased by segregation processes[46]. While the measurement of precise values of segregated planar fault energies is challenging, Eggeler et al. derived an approach to calculate the difference between γ_{APB} and γ_{SISF}[28]. As shown in Supplementary Note 5, this approach yields a difference of at least 46 mJ m^{-2} in the present case. Thus, Eq. 1 cannot be fulfilled even for a near-zero γ_{SISF} as well as negligible friction and misfit forces and the leading Shockley partial dislocation is locked as soon as the configuration is fully segregated.

This argument, however, is only true if the trailing Shockley partial dislocation does not also shear into the γ′ precipitate. Hence, a condition analogous to Eq. 1 is set up for the trailing
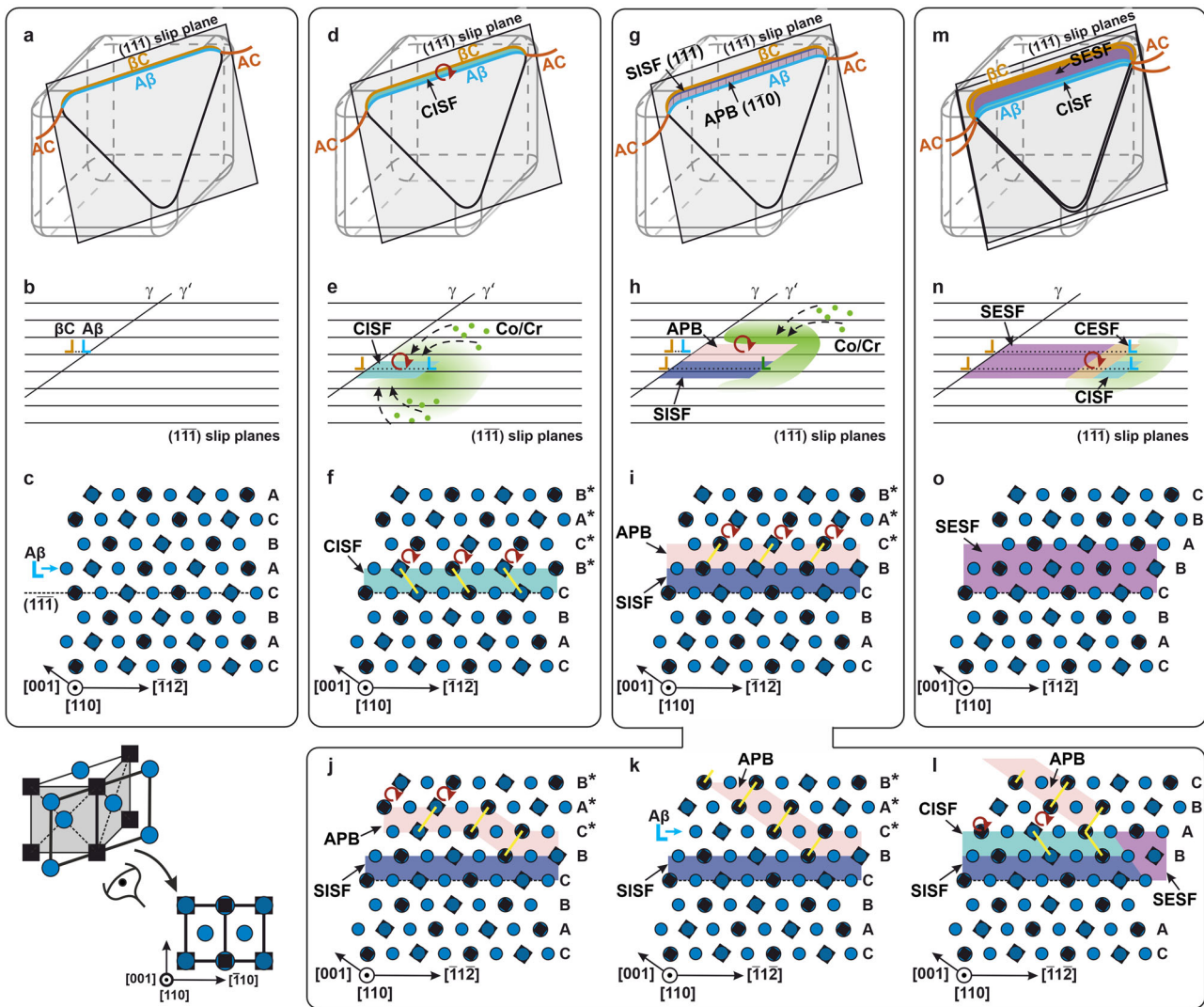
Fig. 5 Nucleation and propagation of superlattice extrinsic stacking faults. The sequence for SESF nucleation and propagation comprises the following steps: **a–c** A dissociated matrix dislocation approaches the γ/γ′ interface. **d–f** The leading Shockley partial dislocation shears into the γ′ precipitate, which is facilitated by the segregation of Co and Cr to the CISF (**e**). As indicated in (**f**), the unfavorable nearest-neighbor relationships can shift to the next (1$\bar{1}$1) plane by atomic reordering along the [110] direction, which is indicated by the red arrow. **g–i** The resulting configuration can be described as an SISF with an APB on top. **j, k** The APB migrates to the (1$\bar{1}$0) plane by atomic reordering to reduce its total energy. **k** As another Shockley partial dislocation (from a second matrix dislocation) approaches this configuration and displaces the upper area by $a/6[\bar{1}1\bar{2}]$, **l** another CISF is created on top of the SISF, which can again reorder to an SISF + APB configuration. By also migrating to the (1$\bar{1}$0) plane, the APB is annihilated by the other APB and a perfect SESF remains. (**m–o**) Both leading Shockley partial dislocations are now able to extend the SESF through the γ′ precipitate facilitated by atomic reordering and segregation of Co and Cr. This sequence is shown in (**a, d, g, m**) as 3D schematic drawings, in (**b, e, h, n**) as 2D schematic drawings focusing on the segregation processes and in (**c, f, i, o**) as schematic drawings of the atomic structure projected along the [110] direction, which reveals the atomic shifts caused by the Shockley partial dislocations and the proposed reordering processes. In the lower left corner, a part of the γ′-(A$_3$B) unit cell and the projected view along the [110] direction for (**c, f, i–l, o**) are shown, whereby the blue circles and black squares represent the A and B sublattices of the L1$_2$ crystal structure.

Shockley partial dislocation (see Supplementary Note 4):

$$\tau b > F_{int} + F_{misfit} + \gamma_{APB} - \gamma_{SISF} + F_f, \quad (2)$$

where F_{int} is the elastic interaction force between the Shockley partial dislocations, which pushes them in opposite directions. Due to the lower Schmid factor of the trailing Shockley partial dislocation, the force per unit length arising from the applied stress only yields $\tau b = R_{p,0.2} m_t b = 579 MPa \cdot 0.236 \cdot 1.46 \cdot 10^{-10} m = 20 mJ\, m^{-2}$. Since the difference between γ_{APB} and γ_{SISF} is at least 46 mJ m^{-2} as determined above, the trailing Shockley partial dislocation cannot shear into the γ′ precipitate even if the other forces are negligible. Thus, the complete defect configuration is immobile.

The inhibition of athermal shearing and bypassing mechanisms by the pinning of matrix dislocations via segregation-assisted

dissociation and planar fault transformation is evidenced by quantifying the defect structures obtained from the TEM investigations using the procedure outlined in ref. [22]. This quantification approach uses the projected stacking fault widths to calculate planar fault densities. Subsequently, these densities can be further used to calculate the share of the plastic strain contributed by specific shearing mechanisms. More details and intermediate calculations can be found in the Methods section and the Supplementary Note 6. As shown in Fig. 6, the share of the plastic strain contributed by stacking fault-based mechanisms is negligible for the higher strain rates of $10^{-3}\,s^{-1}$ and $10^{-4}\,s^{-1}$ at 850 °C. Although shearing by APB-coupled dislocation pairs occurs at these strain rates, plastic deformation is concentrated in
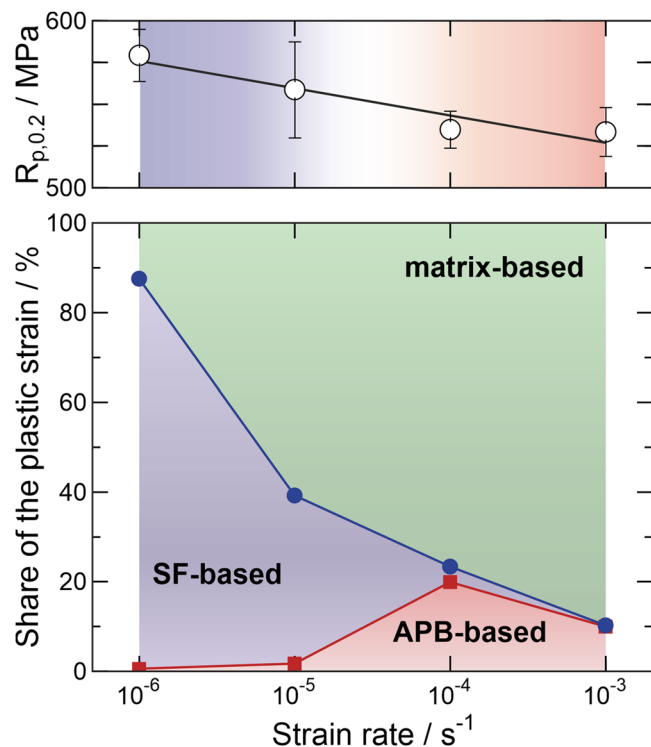
Fig. 6 Significance of stacking fault shearing. Determination of the share of the plastic strain contributed by either APB-based, stacking fault-based or matrix-based deformation as a function of the strain rate at 850 °C. For comparison, the evolution of the yield strength ($R_{p,0.2}$) with strain rate is also included above. Error bars represent the standard deviation.

of superlattice stacking faults in γ′ strengthened superalloys[34,37]. As shown in Supplementary Note 7 using information from refs. [34,37,45,47–49], the calculated propagation velocity of SESFs v_{SESF} is 7.1 nm s^{-1} for ERBOCo-4 at 850 °C. By quantifying additionally the average number of leading dislocation configurations of SESFs n_{LDC} per image area A_{im}, the strain rate provided by SESF shearing $\dot{\varepsilon}_{SESF}$ can be determined as follows:

$$\dot{\varepsilon}_{SESF} = b_z \frac{1}{\tan \theta A_{im}} n_{LDC} v_{SESF} K, \qquad (3)$$

where b_z is the z-component of the combined Burgers vector of the leading Shockley partial dislocations of $a/3[\bar{1}1\bar{2}]$ and θ is the angle between the loading direction and the normal of the glide plane. As the dislocations also shear through the γ matrix channels, which is not assisted by segregation processes and can be assumed to occur nearly instantaneously, a correction factor K is introduced, which is 1.66 for ERBOCo-4 (see Supplementary Note 7 for more details). The resulting calculated strain rates are shown in Supplementary Fig. 9 and compared to the experimentally controlled ones. At higher strain rates, the calculated strain rate provided by SESF shearing is over two orders of magnitude lower than the experimentally specified strain rate, which is in accordance with previous quantification results as stacking fault shearing is far from dominant at these strain rates. As soon as SESF shearing becomes more dominant, the calculated strain rates are in very good agreement with the experimental ones. The slightly higher calculated strain rate of $2.8 \cdot 10^{-6}$ s^{-1} compared to the experimentally set one of 10^{-6} s^{-1} is due to the idealized scenario used for the calculations. In reality, the leading Shockley partial dislocations of SESFs are temporarily impeded at other stacking faults or γ/γ′ interfaces, which decreases their average propagation velocity accordingly. Nevertheless, the very good agreement suggests that stacking fault shearing is indeed completely responsible to accommodate the experimentally set strain rate of the instrument. Hence, SESF shearing does not completely erase the strengthening effect provided by the pinning of the dislocation, so that the stress has to be increased high enough by the instrument to nucleate more SESFs to accommodate the set strain rate due to their too low propagation velocity.

Similar to this mechanism observed under compressive loading, it is conceivable that dislocations may also be pinned at γ/γ′ interfaces during tensile loading. Contrary to compressive loading, the Schmid factor of the leading Shockley partial is only half of that of the trailing one for tensile stresses along the [001] direction. This implies that the trailing Shockley partial is likely to also shear into the γ′ precipitate, creating an APB in its wake. Despite this difference, it is still energetically possible for the CISF to transform into the SISF + APB configuration, pinning the configuration in this process. Nevertheless, the actual occurrence of such transformations and the detailed atomic structure of such configurations are subjects for future investigation.

Considering the operational conditions prevalent in application, single-crystalline alloys typically undergo creep at temperatures well above the yield strength anomaly. Conversely, state-of-the-art polycrystalline superalloys are optimized for performance at comparatively lower temperatures, yet still exceeding 700 °C. During tensile creep at these intermediate temperatures, [011] and [111]-oriented grains of these polycrystalline superalloys deform under the formation of SESFs and microtwins[38]. This deformation behavior mirrors that studied here, i.e., [001] compression of single crystals. Consequently, the mechanism proposed here could also elucidate the transition from athermal shearing to segregation-assisted stacking fault shearing in polycrystalline superalloys. This understanding could

the γ channels and dislocations primarily bypass the γ′ precipitates via Orowan looping, which is consistent with previous investigations[22]. By decreasing the strain rate, the share of the plastic strain contributed by these athermal mechanisms decreases continuously. At the lowest investigated strain rate of 10^{-6} s^{-1}, shearing under stacking fault formation can be attributed to cause 87% of the total plastic strain making it by far the dominant mechanism at this strain rate. This confirms the inhibition of the athermal mechanisms due to the locking of the matrix dislocations at the γ/γ′ interfaces by the proposed mechanism as the yield strength at this low strain rate is even higher than at higher strain rates.

In further support of this argument, our recent study[24] reveals that APB-coupled dislocation pairs remain the dominant deformation mechanism at 850 °C, a strain rate of 10^{-3} s^{-1} and a higher plastic strain of about 1%. Intriguingly, despite a higher applied stress of 745 MPa at a lower strain rate of 10^{-5} s^{-1} (compared to 655 MPa at 10^{-3} s^{-1}), APB-coupled dislocation pairs are only very rarely observed. Based on the experiments at a strain rate of 10^{-3} s^{-1}, the resolved shear stress for shearing by APB-coupled dislocations pairs is reached at considerably lower stress levels. Consequently, this observation strongly suggests that athermal mechanisms are inhibited by a segregation-assisted mechanism, further validating that the transformation of CISFs to SISF + APB configurations pins the dissociated dislocations at the γ/γ′ interfaces.

Interestingly, the complete transition to segregation-assisted shearing under SESF formation does not erase the strengthening effect provided by the pinning of matrix dislocations. As mentioned above, the propagation of SESFs is facilitated by segregation and atomic reordering processes (see Fig. 5n). Recently, Barba et al. derived a model to calculate the propagation velocity

be crucial for advancing alloy design and optimizing performance under operational conditions.

During high temperature deformation of γ′ strengthened superalloys, segregation processes are usually associated with softening, as they lead to a decrease of the planar fault energies, facilitate dislocation propagation and assist microstructural degradation processes by changing the local chemical composition at the planar defects and dislocations[28,31,33,34,37,46,50]. However, by tailoring the alloy composition, the segregation behavior to stacking faults and microtwin boundaries can be modified to trigger a localized phase transformation (LPT) along these defects to the χ ($D0_{19}$) or the η ($D0_{24}$) phase[26,51–55]. These LPTs inhibit more detrimental deformation mechanisms and thus are considered to be an effective strengthening mechanism. By lowering the effective diffusion coefficient in the γ′ precipitates and enabling LPT strengthening, both the magnitude and peak temperature of the yield strength anomaly may be increased, which would also shift the transition from athermal to segregation-assisted shearing to higher temperatures and thus improve the high temperature capabilities of next-generation superalloys.

Conclusion

In this work, the experimentally measured anomalous increase of the yield strength in combination with the HRSTEM(-EDS) investigations and the DFT calculations reveal that segregation processes can also induce another strengthening mechanism by facilitating the dissociation of dislocations at the γ/γ′ interfaces and transforming the resulting CISF to an energetically more favorable but immobile SISF + APB configuration. The transformation to this configuration inhibits athermal deformation mechanisms and leads to a transition to shearing under SESF formation. As the SESF propagation velocity is too low to keep up with the controlled strain rate of the test, the resulting stress increases and more SESFs nucleate, leading to a segregation-assisted yield strength anomaly. The identification of this pinning and planar fault transformation mechanism might pave the way for novel alloy design strategies for all types of γ′ strengthened superalloys including Ni-base, CoNi-base, Co-base and γ′ strengthened multi-principal element alloys with enhanced temperature capabilities.

Methods

Constant strain rate compression tests. A single-crystalline rod of the CoNi-base superalloy ERBOCo-4 (Co-32Ni-8Al-5.7W-6Cr-2.8Ti-1.8Ta-0.4Si-0.1Hf (at.%)) was cast in a laboratory-scale Bridgman furnace, reoriented and heat-treated in a vacuum furnace (1280 °C / 8 h –> 1050 °C / 5 h –> 900 °C / 16 h). As determined by electron backscatter diffraction (*Nordlys* detector from *Oxford Instruments* in a *Zeiss Crossbeam 1540 EsB*), the final misorientation of the rod was lower than 5 ° from [001]. Cylindrical compression specimens with a height of 4.5 mm and a diameter of 3.0 mm were extracted by wire electric discharge machining and the bottom and top surfaces were ground plane-parallel with a tolerance of less than 10 μm using SiC paper up to 2500 grit. Constant strain rate compression experiments parallel to the [001] crystal direction were conducted on an *Instron 4505* electromechanical universal testing machine at temperatures between 800 °C and 950 °C and strain rates between $10^{-2}\,s^{-1}$ and $10^{-6}\,s^{-1}$. For the conventional transmission electron microscopy (CTEM) investigations, experiments were interrupted at a plastic strain of approximately 0.2%. To generate a higher defect and dislocation density, atomic-scale high-resolution scanning transmission electron microscopy (HRSTEM) characterization was conducted on specimens interrupted at a plastic strain of approximately 1.0%.

Transmission electron microscopy. From the center part of the deformed samples, [[001]-oriented foils perpendicular to the loading direction and [110]-oriented ones parallel to it were extracted for TEM and HRSTEM investigations, respectively. The foils were ground to a thickness of 100 μm to 120 μm and electropolished using a 16.7% nitric acid – 83.3% methanol solution in a *Struers Double Jet Tenupol-5* at −25 °C and 40 V. TEM was employed to analyze and quantify the defect structures using a *Philips CM200* at 200 keV. Details on the approach to quantify APB-coupled dislocation pairs and (superlattice) stacking faults can be found in ref. [22]. To acquire a statistically significant result, at least five different TEM bright-field micrographs with a combined analyzed area of at least 25 μm² were evaluated for each specimen. The atomic structure and chemical composition of interfacial dislocations and of the leading Shockley partial dislocation configurations of (superlattice) stacking faults were studied using a double aberration-corrected *Titan Themis*³ equipped with a Super-X energy-dispersive X-ray spectroscopy (EDS) detector at 300 keV. Standard k-factor quantification was applied for the EDS investigations as implemented in the *Velox* software.

Density functional theory calculations. The DFT calculations were performed with the VASP software[56–58] using the generalized gradient approximation[59], projector-augmented wave pseudopotentials[60] and spin-polarization with a plane-wave cut-off of 400 eV and Monkhorst-Pack k-point meshes[61] with a k-point distance of 0.125 Å^{-1}. Starting from a ferromagnetic spin ordering, the atomic positions and supercells were fully relaxed until the forces on each atom are less than 0.01 eV Å^{-1}. The Ni and Co atoms in the $L1_2$ crystal lattice of the supercells with $(Ni,Co)_3Al$ are distributed in an ordered fashion as shown in Fig. 4a on the common sublattice as previous work indicated that sublattice disorder plays only a minor role for segregation to planar faults[62]. The $L1_2$ supercell has 12 layers with 4 atoms in each layer oriented along [$1\bar{1}0$], [$10\bar{1}$], and [111] directions. The defect supercell containing the CISF is created by removing one layer and shifting the layers above by $a/2[\bar{1}10]$. The defect supercell containing the SISF + APB configuration is created accordingly with the APB introduced one layer above the SISF.

Data availability

All datasets generated and analyzed throughout this work are available from the corresponding author upon reasonable request.

References

1. Sato, J. et al. Cobalt-base high-temperature alloys. *Science* **312**, 90–91 (2006).
2. Volz, N. et al. Thermophysical and mechanical properties of advanced single crystalline co-base superalloys. *Metallurg. Mater. Trans. A* **49**, 4099–4109 (2018).
3. Titus, M. S., Suzuki, A. & Pollock, T. M. Creep and directional coarsening in single crystals of new γ–γ′ cobalt-base alloys. *Scripta Materialia* **66**, 574–577 (2012).
4. Neumeier, S., Freund, L. P. & Göken, M. Novel wrought γ/γ′ cobalt base superalloys with high strength and improved oxidation resistance. *Scripta Materialia* **109**, 104–107 (2015).
5. Knop, M. et al. A New Polycrystalline Co-Ni Superalloy. *JOM* **66**, 2495–2501 (2014).

6. Regnier, P. & Dupouy, J. M. Prismatic Slip in Beryllium and the Relative Ease of Glide in H.C.P. Metals. *Phys. Stat. Sol. (b)* **39**, 79–93 (1970).

7. Nortmann, A. & Neuhäuser, H. Investigations on the transition from jerky to viscous glide in CuAl at elevated temperatures. *Mater. Sci. Eng. A* **234–236**, 548–551 (1997).

8. Baker, I. & Gaydosh, D. J. Flow and fracture of Fe-Al. *Mater. Sci. Eng.* **96**, 147–158 (1987).

9. Kawabata, T., Kanai, T. & Izumi, O. Positive temperature dependence of the yield stress in TiAl L10 type superlattice intermetallic compound single crystals at 293–1273 K. *Acta Metallurgica* **33**, 1355–1366 (1985).

10. Stoloff, N. S. & Davies, R. G. The plastic deformation of ordered FeCo and Fe3Al alloys. *Acta Metallurgica* **12**, 473–485 (1964).

11. Flinn, P. A. Theory of deformation in superlattices. *Trans. Am. Inst. Mining Metallurg. Eng.* **218**, 145–154 (1960).

12. Westbrook, J. H. Temperature dependence of the hardness of secondary phases common in turbine bucket alloys. *JOM* **9**, 898–904 (1957).

13. Kear, B. H. & Wilsdorf, H. G. F. Dislocation configurations in plastically deformed Cu3Au alloys. *Trans. Metallurg. Soc. AIME* **224**, 382–386 (1962).

14. Kear, B. H. Dislocation configurations and work hardening in Cu3Au crystals. *Acta Metallurgica* **12**, 555–569 (1964).

15. Veyssière, P. & Saada, G. Chapter 53: Microscopy and plasticity of the L12 γ′ phase. in *Dislocations in Solids* vol. 10 253–441 (Elsevier, 1996).

16. Takeuchi, S. & Kuramoto, E. Temperature and orientation dependence of the yield stress in Ni3Ga single crystals. *Acta Metallurgica* **21**, 415–425 (1973).

17. Suzuki, A. & Pollock, T. M. High-temperature strength and deformation of γ/γ′ two-phase Co–Al–W-base alloys. *Acta Materialia* **56**, 1288–1297 (2008).

18. Shi, L., Yu, J. J., Cui, C. Y. & Sun, X. F. Temperature dependence of deformation behavior in a Co–Al–W-base single crystal superalloy. *Mater. Sci. Eng. A* **620**, 36–43 (2015).

19. Barba, D., Egan, A. J., Gong, Y., Mills, M. J. & Reed, R. C. Rationalisation of the Micromechanisms Behind the High-Temperature Strength Limit in Single-Crystal Nickel-Based Superalloys. in *Superalloys 2020 (Proceedings 14th Int. Symp. Superalloys)* 260–272 (2020).

20. Suzuki, A., DeNolf, G. C. & Pollock, T. M. Flow stress anomalies in γ/γ′ two-phase Co–Al–W-base alloys. *Scripta Materialia* **56**, 385–388 (2007).

21. Fan, Z. et al. The temperature dependence of high-temperature strength and deformation mechanism in a single crystal CoNi-base superalloy. *Mater. Sci. Eng. A* **735**, 114–120 (2018).

22. Bezold, A. et al. Quantification of the temperature-dependent evolution of defect structures in a CoNi-base superalloy. *Acta Materialia* **227**, 117702 (2022).

23. Bezold, A. et al. Yielding behavior of a single-crystalline γ′-strengthened Co-Ti-Cr superalloy. *Scripta Materialia* **200**, 113928 (2021).

24. Vollhüter, J. et al. Strain rate-dependent anomalous work hardening of a single-crystalline CoNi-base superalloy. *Metall. Mater. Trans. A* **54**, 1608–1619 (2023).

25. Viswanathan, G. B. et al. Segregation at stacking faults within the γ′ phase of two Ni-base superalloys following intermediate temperature creep. *Scripta Materialia* **94**, 5–8 (2015).

26. Smith, T. M. et al. Segregation and η phase formation along stacking faults during creep at intermediate temperatures in a Ni-based superalloy. *Acta Materialia* **100**, 19–31 (2015).

27. Titus, M. S., Eggeler, Y. M., Suzuki, A. & Pollock, T. M. Creep-induced planar defects in L12-containing Co- and CoNi-base single-crystal superalloys. *Acta Materialia* **82**, 530–539 (2015).

28. Eggeler, Y. M. et al. Planar defect formation in the γ′ phase during high temperature creep in single crystal CoNi-base superalloys. *Acta Materialia* **113**, 335–349 (2016).

29. Titus, M. S. et al. Solute segregation and deviation from bulk thermodynamics at nanoscale crystalline defects. *Sci. Adv.* **2**, e1601796 (2016).

30. Kontis, P. et al. The effect of chromium and cobalt segregation at dislocations on nickel-based superalloys. *Scripta Materialia* **145**, 76–80 (2018).

31. Makineni, S. K. et al. On the diffusive phase transformation mechanism assisted by extended dislocations during creep of a single crystal CoNi-based superalloy. *Acta Materialia* **155**, 362–371 (2018).

32. Lenz, M., Wu, M. & Spiecker, E. Segregation-assisted climb of Frank partial dislocations: An alternative route to superintrinsic stacking faults in L12-hardened superalloys. *Acta Materialia* **191**, 270–279 (2020).

33. Titus, M. S. et al. High resolution energy dispersive spectroscopy mapping of planar defects in L1 2 -containing Co-base superalloys. *Acta Materialia* **89**, 423–437 (2015).

34. Barba, D. et al. On the microtwinning mechanism in a single crystal superalloy. *Acta Materialia* **135**, 314–329 (2017).

35. Vorontsov, V. A., Kovarik, L., Mills, M. J. & Rae, C. M. F. High-resolution electron microscopy of dislocation ribbons in a CMSX-4 superalloy single crystal. *Acta Materialia* **60**, 4866–4878 (2012).

36. Karpstein, N. et al. Reliable identification of the complex or superlattice nature of intrinsic and extrinsic stacking faults in the L12 phase by high-resolution imaging. *Acta Materialia* **260**, 119284 (2023).

37. Barba, D., Smith, T. M., Miao, J., Mills, M. J. & Reed, R. C. Segregation-assisted plasticity in Ni-based superalloys. *Metallurg. Mater. Trans. A* **49**, 4173–4185 (2018).

38. León-Cázares, F. D., Monni, F. & Rae, C. M. F. Stress orientation dependence for the propagation of stacking faults and superlattice stacking faults in nickel-based superalloys. *Acta Materialia* **199**, 209–224 (2020).

39. Viswanathan, G. B. et al. Investigation of creep deformation mechanisms at intermediate temperatures in René 88 DT. *Acta Materialia* **53**, 3041–3057 (2005).

40. Smith, T. M., Unocic, R. R., Deutchman, H. & Mills, M. J. Creep deformation mechanism mapping in nickel base disk superalloys. *Mater. High Temp.* **33**, 372–383 (2016).

41. Bezold, A. et al. Deformation mechanisms in compositionally complex polycrystalline CoNi-base superalloys: influence of temperature, strain-rate and chemistry. *Metall. Mater. Trans. A* **54**, 1649–1660 (2023).

42. Bezold, A. & Neumeier, S. Tailoring deformation mechanisms in polycrystalline CoNi-base superalloys for enhanced high temperature strength. *Scripta Materialia* **226**, 115250 (2023).

43. Lenz, M. et al. Atomic Structure and Chemical Composition of Planar Fault Structures in Co-Base Superalloys. in *Superalloys 2020 (Proceedings 14th Int. Symp. Superalloys)* 920–928 (2020).

44. Kolbe, M. The high temperature decrease of the critical resolved shear stress in nickel-base superalloys. *Mater. Sci. Eng. A* **319–321**, 383–387 (2001).

45. Kovarik, L. et al. Microtwinning and other shearing mechanisms at intermediate temperatures in Ni-based superalloys. *Progr. Mater. Sci.* **54**, 839–873 (2009).

46. Feng, L. et al. Shearing of γ′ particles in Co-base and Co-Ni-base superalloys. *Acta Materialia* **161**, 99–109 (2018).

47. Volz, N. et al. Creep properties and deformation mechanisms of single-crystalline γ′-strengthened superalloys in dependence of the Co/Ni ratio. *Philosoph. Mag.* **102**, 718–744 (2022).

48. Freund, L. Mikrostrukturelle und mechanische Charakterisierung von polykristallinen ausscheidungsgehärteten Co-Basis Superlegierungen unter besonderer Berücksichtigung der Verformungsmechanismen. (FAU University Press, 2018).

49. Asaro, R. J. & Suresh, S. Mechanistic models for the activation volume and rate sensitivity in metals with nanocrystalline grains and nano-scale twins. *Acta Materialia* **53**, 3369–3382 (2005).

50. Lenz, M. et al. Tension/Compression asymmetry of a creep deformed single crystal Co-base superalloy. *Acta Materialia* **166**, 597–610 (2019).

51. Smith, T. M. et al. Phase transformation strengthening of high-temperature superalloys. *Nat. Commun.* **7**, 13434 (2016).

52. Smith, T. M. et al. Effect of stacking fault segregation and local phase transformations on creep strength in Ni-base superalloys. *Acta Materialia* **172**, 55–65 (2019).

53. Egan, A. J. et al. Effect of Nb Alloying Addition on Local Phase Transformation at Microtwin Boundaries in Nickel-Based Superalloys. in *Superalloys 2020 (Proceedings 14th Int. Symp. Superalloys)* 640–650 (2020).

54. Smith, T. M. et al. Utilizing local phase transformation strengthening for nickel-base superalloys. *Commun. Mater.* **2**, 106 (2021).

55. Egan, A. J. et al. Local Phase Transformation Strengthening at Microtwin Boundaries in Nickel-Based Superalloys. *Acta Materialia* **238**, 118206 (2022).

56. Kresse, G. & Furthmüller, J. Efficiency of ab-initio total energy calculations for metals and semiconductors using a plane-wave basis set. *Comput. Mater. Sci.* **6**, 15–50 (1996).

57. Kresse, G. & Furthmüller, J. Efficient iterative schemes for ab initio total-energy calculations using a plane-wave basis set. *Phys. Rev. B* **54**, 11169–11186 (1996).

58. Kresse, G. & Joubert, D. From ultrasoft pseudopotentials to the projector augmented-wave method. *Phys. Rev. B* **59**, 1758–1775 (1999).

59. Perdew, J. P., Burke, K. & Ernzerhof, M. Generalized Gradient Approximation Made Simple. *Phys. Rev. Lett.* **77**, 3865–3868 (1996).

60. Blöchl, P. E. Projector augmented-wave method. *Phys. Rev. B* **50**, 17953–17979 (1994).

61. Monkhorst, H. J. & Pack, J. D. Special points for Brillouin-zone integrations. *Phys. Rev. B* **13**, 5188–5192 (1976).

62. Volz, N. et al. Understanding creep of a single-crystalline Co-Al-W-Ta superalloy by studying the deformation mechanism, segregation tendency and stacking fault energy. *Acta Materialia* **214**, 117019 (2021).

Acknowledgements

Author contributions

A.B. and S.N. designed the study. A.B. and J.V. carried out the TEM investigations and compression experiments. N.K. and M.L. performed the HRSTEM(-EDS) investigations. A.B., J.V., C.Z., N.K., E.S. and S.N. analyzed the experimental data and developed the proposed mechanism. A.S. and T.H. conducted the DFT calculations. S.N., M.G. and E.S. supervised the project. A.B. wrote the paper and all authors contributed to the discussion and revision of the paper.

Competing interests

The authors declare no competing interests.

Additional information

Supplementary information The online version contains supplementary material available at https://doi.org/10.1038/s43246-024-00447-x.

Correspondence and requests for materials should be addressed to Andreas Bezold.

Peer review information *Communications Materials* thanks the anonymous reviewers for their contribution to the peer review of this work. Primary Handling Editor: John Plummer. A peer review file is available.

Reprints and permission information is available at http://www.nature.com/reprints

Publisher's note Springer Nature remains neutral with regard to jurisdictional claims in published maps and institutional affiliations.